WIND-INDUCED RESPONSE OF FLAT-ELLIPTICAL PIPE GREENHOUSES: A COMPARATIVE STUDY OF CONTACT AND BINDING MODELS

/

平椭圆管塑料大棚风振响应分析：接触模型与绑定模型对比研究

Cunxing WEI[1)], Hengyan XIE[2,*)], Xin ZHENG[2)], Wenbao XU[2)]

[1)] College of Engineering, Heilongjiang Bayi Agricultural University, Daqing 163319 / China;

[2)] College of Civil Engineering and Water Conservancy, Heilongjiang Bayi Agricultural University, Daqing 163319 / China

Tel: +86-459-13766785587; E-mail: xiehy555@byau.cn

Corresponding author: Hengyan Xie

DOI: https://doi.org/10.35633/inmateh-78-24

Keywords: *flat-elliptical pipe greenhouse; time-history analysis; finite element contact; fluctuating wind; wind-induced vibration responses*

ABSTRACT

This study addresses the limitations in current finite element analysis (FEA) models of wind-induced response in plastic greenhouses, focusing on the oversimplification of modeling and the neglect of fluctuating wind effects. By deriving dynamic equations of motion for the greenhouse under wind loading and incorporating fluctuating wind through the Davenport wind speed spectrum, the study uses ABAQUS software to create both binding and contact models for a flat-elliptical pipe greenhouse (FEPG). The results emphasize the significant impact of fluctuating wind and the interactions between structural components on wind-induced responses. This work contributes to the design of more resilient greenhouses by enhancing the accuracy of wind response predictions, thereby improving the theoretical framework for FEPG design and providing a more comprehensive approach to wind-induced vibration analysis.

摘要

本研究针对当前塑料大棚风致响应有限元分析（FEA）模型中存在的过度简化建模和忽视脉动风效应的问题展开。通过推导温室在风荷载下的动态运动方程，并采用 Davenport 风速谱模拟脉动风，利用 ABAQUS 软件建立了平椭圆管塑料大棚（FEPG）的约束模型和接触模型。研究结果表明，脉动风和结构部件之间的相互作用对风致响应有显著影响。本研究通过提高风致响应预测的准确性，为温室设计提供了更为可靠的理论支持，进一步完善了 FEPG 设计理论框架，并为风致振动分析提供了更全面的方法。

INTRODUCTION

Plastic greenhouses, widely used in modern agriculture, have become an essential facility for greenhouse cultivation due to their lightweight structure, excellent thermal insulation properties, and low construction cost *(Reichrath, 2002; Kim, 2019)*. However, in recent years, the increasing frequency of extreme climate events, particularly the effects of strong winds, has led to the collapse of numerous greenhouses, resulting in severe economic losses *(Briassoulis, 2016; Kwon, 2016; Ryu, 2019; Wei, 2025a)*. These phenomena highlight the shortcomings of current greenhouse design methods, which largely rely on empirical formulas and lack comprehensive dynamic analysis and precise evaluation of structural responses under extreme wind loads.

Although progress has been made in recent years on the wind-induced responses of greenhouse frames and covering materials, the dynamic coupling mechanisms between the film, film-tensioning lines, and frame remain unclear *(Richardson, 1986; Ren, 2019; Dougka, 2010; Xie, 2025; Wei, 2025b)*. Existing studies have primarily focused on the stability and load-bearing capacity of the frame, neglecting the complex interactions among these components, particularly under fluctuating wind loads *(Wells, 1980; Reichrath, 2002; Li, 2022; Wang, 2022, 2023; Xu, 2023)*. These factors, which significantly influence the overall structural response, have not received adequate attention. As a result, relying on static load analyses or simplified modeling approaches is inadequate for accurately assessing the safety and reliability of greenhouse structures under extreme weather conditions.

Cunxing Wei, Ph.D. Eng.; Hengyan Xie, Prof. Ph.D. Eng.; Xin Zheng, Prof. Ph.D. Eng.; Wenbao Xu, Ph.D. Eng.

To address this gap, the objective of this study is to investigate the dynamic coupling effects between the film, film-tensioning lines, and frame under fluctuating wind loads through time-history analysis. Unlike traditional static analysis methods, this study uses time-history analysis to simulate the dynamic deformation and contact behavior of the structure under fluctuating wind loads, revealing the complex interactions between the film, film-tensioning lines, and frame. The specific objectives of this study are as follows:

(1) To develop a dynamic model that comprehensively considers the interactions between the film, film-tensioning lines, and frame.

(2) To investigate the impact of fluctuating wind loads on the greenhouse structure, particularly the complex dynamic coupling effects between the film, film-tensioning lines, and frame.

(3) To perform a time-history analysis, providing the first-ever systematic investigation of the dynamic coupling effects of fluctuating wind loads on the entire system of film, film-tensioning lines, and frame.

(4) To provide scientific basis for wind-resistant design of greenhouses under extreme climatic conditions, offering new perspectives for the design optimization and safety evaluation of greenhouse structures, particularly in fine-scale evaluations under fluctuating wind loads.

The novelty of this study lies in performing the first dynamic time-history analysis of the entire system comprising the film, film-tensioning lines, and frame, and revealing the dynamic effects of fluctuating wind loads on the overall structural response. This innovative approach not only uncovers the complex dynamic coupling effects between the film, film-tensioning lines, and frame but also provides a scientific foundation for the wind-resistant design of greenhouses under extreme climatic conditions, holding significant practical application value.

MATERIALS AND METHODS

Establishment of dynamic equilibrium equation

The time-domain analysis approach is employed for the wind-induced vibration analysis of the flat-elliptical pipe greenhouse (FEPG) structures. The wind load time history is derived using the linear filtering method, which is a well-established technique, and has been previously studied by the authors. For this study, modifications to the method are necessary to address the contact interactions. This section provides a comprehensive description of the wind-induced vibration analysis method, taking into account the contact between the frame, film, and film-tensioning lines. When the greenhouse components are modeled as a unified structural system, the governing equation of structural dynamics can be written as:

$$M\ddot{u}(t) + C\dot{u}(t) + Ku(t) = F(t) \tag{1}$$

where: M, C and K is the mass matrix, damping matrix and stiffness matrix of the integrated structure, respectively; $\ddot{u}(t)$, $\dot{u}(t)$ and $u(t)$ is the acceleration, velocity, and displacement vectors of the integrated structure at time t, respectively; $F(t)$ is the external load vector acting on the integrated structure at time t.

In previous studies, the finite element model often simplified the system by combining the film-tensioning line, film, and frame into a single component. In such models, these elements were treated as a unified entity, considering only their equivalent stiffness; this simplification is referred to as the binding model. Under this approach, the governing equation in Eq. (1) is applicable. However, in real-world applications, the contact interactions between the film-tensioning line, film and frame-such as adhesion, slippage, and separation-cannot be ignored.

When the contact model is adopted for wind-induced vibration analysis, an additional contact force must be included on the right-hand side of the governing equation to capture the interactions between the film-tensioning line, film, and frame. Moreover, the prestress in the film and film-tensioning line contributes to additional structural stiffness, as expressed in Eq. (3).

$$M\ddot{u}(t) + C\dot{u}(t) + K_{total}u(t) = F(t) + F_{contact} \tag{2}$$

$$K_{total} = K_0 + K_f + K_l \tag{3}$$

where:

$F_{contact}$ is the total contact force among the frames, film, and film-tensioning lines; K_{total} is the total stiffness of the structure; K_0 is the original stiffness matrix of the structure, corresponding to the stiffness without considering the prestress; K_f is the stiffness matrix induced by the prestress of the film; K_l is the stiffness matrix arising from the prestress along the compression of the line.

The equation governing the equilibrium of tangential forces acting on the film within the structure is as follows:

$$F_{contact} = F_{contact\_s} + F_{contact\_l} \tag{4}$$

$$F_{contact-s} = \begin{bmatrix} f_n & f_x & f_y \end{bmatrix} \tag{5}$$

where: $F_{contact}$ is the total contact force among the frames, film, and film-tensioning lines; $F_{contact-s}$ is the contact force between the frames and the film; $F_{contact-l}$ is the contact force between the film-tensioning lines and the film; f_n is the normal contact force between two contacting bodies; f_x is the contact force in the x-direction between two contacting bodies; f_y is the contact force in the y-direction between two contacting bodies.

$$f_n = \begin{cases} 0 & when \quad u_n > 0 \\ k_n u_n + \lambda_{i+1} & when \quad u_n \le 0 \end{cases} \tag{6}$$

$$\lambda_{i+1} = \begin{cases} \lambda_{i+1} + k_n u_n & when \quad u_n > \varepsilon \\ \lambda_i & when \quad u_n \le \varepsilon \end{cases} \tag{7}$$

where: k_n is the normal contact stiffness; u_n is the contact gap; ε is invasion tolerance; λ_i is the components of Lagrange multipliers of iteration step i for each iteration element.

Based on Coulomb's law, three contact states are considered. The first is the separation state, where the tangential contact force f_x equals zero. The second is the sticking state, where the tangential contact force f_x is less than the critical friction force. The third is the sliding state, in which f_x reaches the critical friction force, and the film-tensioning line begins to slip. The friction f_x is as follows (f_y is similar):

$$f_x = \begin{cases} k_s u_x & when \quad u_n \le 0 \quad and \quad f = \sqrt{f_x^2 + f_y^2} - \mu f_n < 0 \\ \mu f_n & when \quad u_n \le 0 \quad and \quad f = \sqrt{f_x^2 + f_y^2} - \mu f_n = 0 \\ 0 & when \quad u_n > 0 \end{cases} \tag{8}$$

where: k_s is the tangential contact stiffness; u_x is the slip contact distance in the x direction; μ is the coefficient of friction.

Thus, the equation of motion that accounts for the contact interactions between structural components, as well as the prestress in the film-tensioning lines and film, can be expressed as follows:

$$\begin{bmatrix} M_s & 0 & 0 \\ 0 & M_f & 0 \\ 0 & 0 & M_l \end{bmatrix} \begin{Bmatrix} \ddot{u}_1(t) \\ \ddot{u}_2(t) \\ \ddot{u}_3(t) \end{Bmatrix} + \begin{bmatrix} C_s & 0 & 0 \\ 0 & C_f & 0 \\ 0 & 0 & C_l \end{bmatrix} \begin{Bmatrix} \dot{u}_1(t) \\ \dot{u}_2(t) \\ \dot{u}_3(t) \end{Bmatrix} + \begin{bmatrix} K_0 & 0 & 0 \\ 0 & K_f & 0 \\ 0 & 0 & K_l \end{bmatrix} \begin{Bmatrix} u_1(t) \\ u_2(t) \\ u_3(t) \end{Bmatrix} = \begin{bmatrix} F(t) + F_{contact-s} \\ F(t) + F_{contact-s} + F_{contact-l} \\ F(t) + F_{contact-l} \end{bmatrix} \tag{9}$$

where: M_s, M_f, M_l is the mass matrix of frame, film and film-tensioning line, respectively; C_s, C_f, C_l is the damping matrix of frame, film and film-tensioning line, respectively; K_s, K_f, K_l is the stiffness matrix of frame, film and film-tensioning line, respectively; $\ddot{u}$, $\dot{u}$, u is the nodal acceleration vector, nodal velocity vector and nodal displacement vector.

Finite element model

Material parameter

The frame of the greenhouse was assembled from Q235B galvanized steel pipes due to their superior strength, stiffness, and resistance to corrosion, thereby maintaining structural integrity under wind-induced loading. The greenhouse was clad with polyolefin (PO) film, chosen for its toughness, ductility, high light transmittance, thermal insulation, and durability. Film-tension line was maintained using polyamide (PA, nylon) lines, capable of sustaining substantial tensile forces to ensure membrane stability.

The material parameters of the frame, film, and film-tensioning line were carefully selected for optimal structural performance. The frame of the greenhouse consists of Q235B steel, with the rafters having dimensions of 30×60 mm and a thickness of 2 mm, while the embedded steel pipes have dimensions of 30×80 mm and a thickness of 2 mm. Both materials have a density of 7.85 kg/m³, a yield strength of 235 MPa, a Poisson's ratio of 0.28, and an elastic modulus of 2.1×10^5 MPa. The purlins are also made of Q235B steel, with a diameter of 20 mm and a thickness of 2 mm, maintaining the same material properties. The film used for covering the greenhouse has a thickness of 0.12 mm and a density of 0.94 kg/m³, with a Poisson's ratio of 0.44 and an elastic modulus of 500 MPa. Finally, the film-tensioning line is constructed from steel with dimensions of 20×2 mm, featuring a density of 1.15 kg/m³, a Poisson's ratio of 0.35, and an elastic modulus of 3500 MPa.

Contact model building

In this research, two finite element models were developed using ABAQUS software, focusing on the contact interactions and binding conditions involving the film, film-tensioning line, and frame. The models were subjected to identical boundary conditions for consistency. The rafter feet are typically welded to the bottom steel pipes in real-world scenarios, creating a stiff support system. In the finite element models, this connection was treated as fixed, restricting all translations and rotations at the bottom steel pipes.

For the discretization of the frame, C3D8R solid elements were employed. These 8-node hexahedral elements use reduced integration and provide three degrees of freedom at each node, offering superior resistance to shear locking under bending and high accuracy in displacement solutions, even when the mesh undergoes distortion. The film was represented by M3D4R membrane elements, which are 4-node linear quadrilateral elements. These elements are particularly suitable for simulating thin films that are only subjected to in-plane tension and do not exhibit bending stiffness. The B31 element, a 2-node beam element, was used for modeling the film-tensioning line. With three degrees of freedom at each node, this element is ideal for simulating axial forces, as it lacks bending resistance, which aligns with the assumptions made in this study. Given that both M3D4R and B31 elements capture large deformations and demonstrate geometrically nonlinear behavior, geometric nonlinearity was included in the analysis.

In the binding model, the film-tensioning lines, film, and frame are interconnected through binding connections, which restrict their relative degrees of freedom to 0, as shown in Fig. 1(a). In the contact model, the film-tensioning lines, film, and frame are connected through contact interactions, releasing the relative degrees of freedom between them while allowing the contact forces. Specifically, the contact between the frame and the film is modeled as a point-to-surface interaction, where nodes on the frame are connected to the film surface.

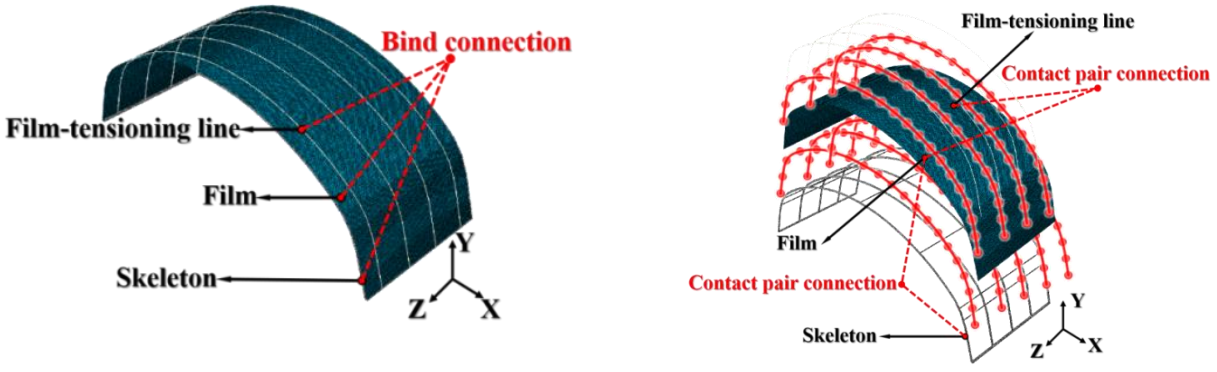

a) Binding model *b) Contact model*

Fig. 1 – Schematic diagram of the different connection methods

Similarly, the interaction between the film-tensioning lines and the film is also modeled as a point-to-surface contact, with nodes on the film-tensioning lines connected to the film surface, as illustrated in Fig. 1(b).

In this study, the dynamic behavior of the flat-elliptical pipe greenhouse (FEPG) was analyzed using both a binding model and a contact model. The contact parameters (friction coefficient μ and normal stiffness k_n) are critical for accurately simulating the interaction between the greenhouse components. The friction coefficient is assumed to be 0.52, based on previous experimental studies of contact between PO films and steel components *(Wei, 2025a)*. The normal stiffness was derived from the material properties of the film and frame, accounting for the prestress in the system.

Simulation of fluctuating wind speed

Drawing on prior research and multiple experiments with varying parameters, the simulation settings for fluctuating wind speed were determined as follows: (1) The mean wind speed at a 10-meter height with a 10-year recurrence interval in Jiamusi, Heilongjiang Province, is 27.88 m/s *(MOHURD, 2016)*; (2) The autoregressive model order was set to 4; (3) The total simulation time was 60 seconds, with a time step of 0.1 seconds; (4) The upper frequency cutoff was 10 Hz, and the frequency step was 0.01 Hz; (5) The surface drag coefficient K was 0.003.

The fluctuating wind speed was simulated using the Davenport wind speed spectrum, chosen for its conservative approach to high-frequency wind components. The comparison with the Kaimal and Von Karman spectra confirmed that the Davenport model is better suited for the wind characteristics of Heilongjiang Province, especially considering the high-frequency wind components that influence the structure's response. To simulate the fluctuating wind perpendicular to the greenhouse surface, the Davenport fluctuating wind power spectrum *(Davenport, 1961)* was applied, as given by:

$$S_v(f) = \overline{V}_{10}^2 \frac{4Kx}{f(1+x^2)^{4/3}} \tag{10}$$

$$x = 1200\frac{f}{\overline{V}_{10}} \tag{11}$$

where: $S_v(f)$ is the auto-power of the fluctuating wind speed, f is the fluctuating wind speed frequency, K is the surface drag coefficient, $\bar{V}_{10}$ is the mean wind speed at 10-meter height with 10-minute interval, x is the integral scale coefficient of turbulence, which is 0.02 in Davenport fluctuating wind speed spectrum.

Based on the aforementioned conditions, Fig. 2(a) shows the simulated fluctuating wind velocity at a height of 10 m over a duration of 60 s. The simulated wind velocity fluctuates around zero, exhibiting the characteristics of a stationary stochastic process. Fig. 2(b) presents a comparison between the power spectral density (PSD) of the simulated wind velocity and the Davenport spectrum. It can be observed that the simulated PSD matches the Davenport spectrum well, indicating that the simulated wind velocity is reliable and suitable for use in the wind-induced dynamic response analysis of the FEPG structure.

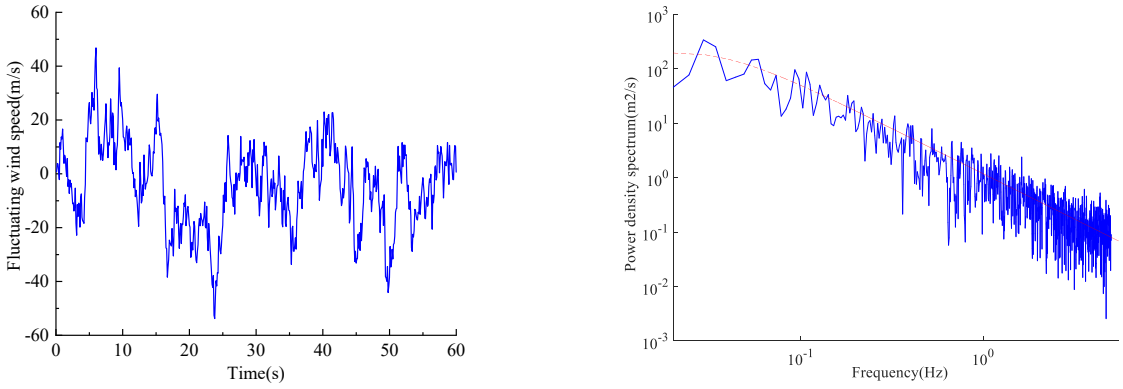

a) Fluctuating wind speed at 10 m height

b) Comparison between simulated spectrum and Davenport spectrum

Fig. 2 – Simulated fluctuating wind speed and spectrum comparison

Generation of full dynamic wind loads

Once the fluctuating wind velocity is determined, it is combined with the mean wind velocity to calculate the full dynamic wind velocity. Using the Bernoulli equation, this full dynamic wind velocity can be converted into the corresponding dynamic wind pressure acting on the structure.

According to the Chinese standard *(MOHURD, 2016)*, the wind load perpendicular to the greenhouse surface is calculated as follows when analyzing the primary greenhouse structure:

$$w_k = \mu_s \mu_z w \tag{12}$$

where: w_k is the standard value of the wind load (kN/m^2); μ_S is the shape coefficient of wind pressure; μ_Z is the height variation coefficient of the wind pressure; w is the wind pressure acting on structure (kN/m^2), and here it is the full dynamic wind pressure.

RESULTS AND DISCUSSION

Wind-induced vibration responses of film

To investigate the stress and displacement wind-induced responses of the film under full dynamic wind load, the stress time history curves at the peak stress node and the displacement time history curves at the peak displacement node of both the binding model and the contact model are extracted and presented in the Fig. 3.

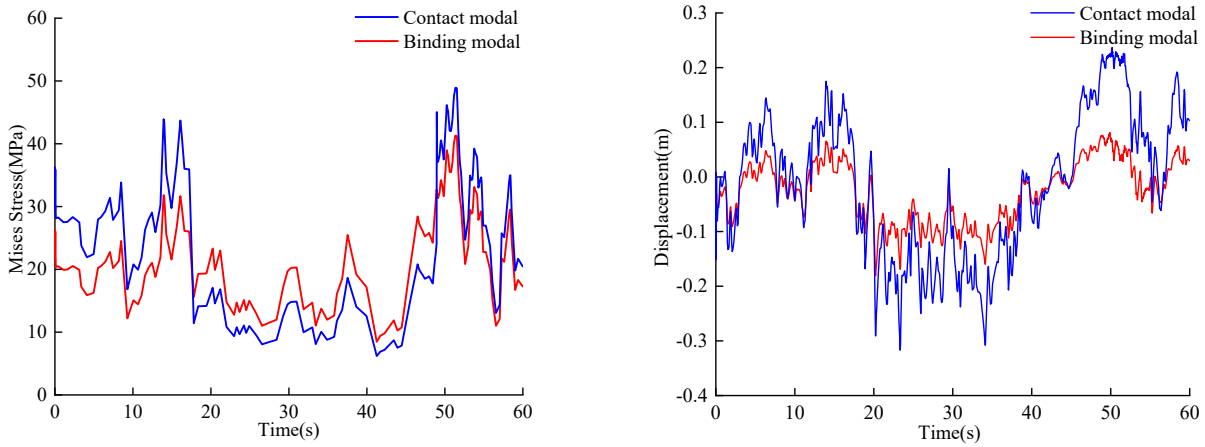

a) Stress time history curves *b) Displacement time history curves*

Fig. 3 – Stress and displacement time history curves of film

The maximum stress nodes on the film of both the contact and binding models are located in the shoulder region on the windward side of the film. As illustrated in the Fig. 3(a), the stress at these peak nodes fluctuates with a similar trend observed for both models. In contrast to the stress time curves for the frame and film-tensioning line, the stress time curve for the peak stress points of the contact model fluctuates around the curve of the binding model. The peak stress values for both the contact and binding models occur at 51.4 s. At this time, the maximum stress in the contact model is 48.85 MPa, while in the binding model, it is 41.28 MPa, with the maximum stress in the contact model approximately 1.18 times that in the binding model.

The maximum displacement nodes on the film of both the contact and binding models are located in the shoulder region on the leeward side of the film. As shown in the Fig. 3(b), the displacement time curve for the peak displacement nodes of the contact model fluctuates around the displacement time curve of the binding model, with a larger amplitude of fluctuation. The peak displacements for both the contact and binding models occur at 50.19 s. At this time, the displacement in the contact model is 232.1 mm, while in the binding model, the displacement is 79.2 mm. The maximum displacement in the contact model is approximately 2.93 times that of the binding model.

The results indicate a substantial difference between the contact and binding models, particularly in the displacement and stress magnitudes. This difference is primarily due to the incorporation of the film-frame interaction in the contact model, which is more reflective of real-world conditions. The higher stress and displacement values observed in the contact model underscore the importance of considering structural interactions when evaluating wind-induced responses in plastic greenhouses.

These findings are consistent with previous studies, such as *Wei(2025a)*, who also noted that accounting for the interaction between the greenhouse covering and structural components leads to more accurate results in stress analysis.

Wind-induced vibration responses of frame

To investigate the stress and displacement wind-induced responses of the frame under full dynamic wind load, the stress time history curves at the peak stress node and the displacement time history curves at the peak displacement node of both the binding model and the contact model are extracted and presented in the Fig. 4 and Fig. 5.

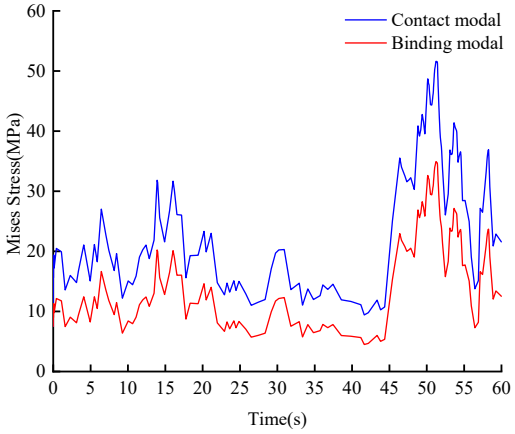

Fig. 4 – Stress time history curves of frame

The maximum stress nodes on the frame of both the contact and binding models are located in the shoulder region on the windward side of the center frame. As illustrated in Fig. 4, the stress at these peak nodes fluctuates with a similar trend observed for both models. The peak stress values for both the contact and binding models occur at 51.4 s. At this time, the maximum stress in the contact model is 51.36 MPa, while in the binding model, it is 34.64 MPa, with the maximum stress in the contact model approximately 1.48 times that in the binding model.

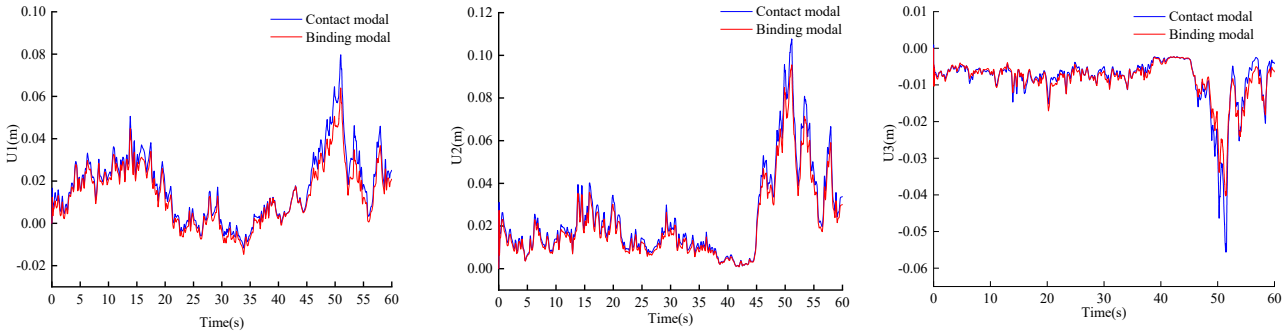

a) X-direction ***b) Y-direction*** ***c) Z-direction***

Fig. 5 – Displacement time history curves of frame

The maximum displacement nodes on the frame of both the contact and binding models are located in the shoulder region on the leeward side of the center frame. As shown in the Fig. 5, the displacement at these peak nodes varies with a similar trend observed for both models. The peak displacements for both the contact and binding models occur at 51.4 s. At this time, the displacement components for the contact model are 79.6 mm in the x-direction, 107.6 mm in the y-direction, and 55.6 mm in the z-direction. For the binding model, the displacement components are 63.7 mm in the x-direction, 95.3 mm in the y-direction, and 40.2 mm in the z-direction. The maximum displacement components in the x, y and z directions for the contact model are 1.25, 1.13, and 1.38 times those of the binding model, respectively.

The stress and displacement results for the frame show a consistent trend, with the contact model yielding higher values than the binding model. The observed increases in stress and displacement, particularly in the contact model, align with the findings of *Wei (2025a)*, who demonstrated that accounting for structural interactions significantly impacts the response of greenhouse frameworks to dynamic wind loads. Moreover, the results suggest that for typical greenhouse structural materials (which typically have allowable stress limits around 40-50 MPa), the higher stress values in the contact model (up to 51.36 MPa) might require reevaluation of material choices or reinforcement strategies in actual designs.

Wind-induced vibration responses of film-tensioning line

To examine the wind-induced stress and displacement responses of the film-tensioning line under full dynamic wind load, the stress time history at the peak stress node and the displacement time history at the peak displacement node are extracted for both the binding and contact models. These are presented in Fig.6 and Fig.7.

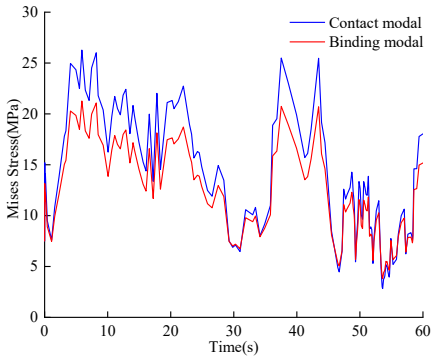

Fig. 6 – Stress time history curves of film-tensioning line

The maximum stress nodes on the film-tensioning line of both the contact and binding models are located from the top of the second film-tensioning line to the shoulder region on the leeward side. As shown in the Fig. 6, the stress at these peak nodes fluctuates over time, with a similar variation trend observed for both models. This variation is closely related to the wind pressure time history acting on the FEPG, exhibiting a pattern of initially increasing, then decreasing, and increasing again. The peak stresses for both the contact and binding models occur at 5.91 s. At this time, the maximum stress in the contact model is 26.27 MPa, while in the binding model, it is 21.26 MPa, with the maximum stress in the contact model approximately 1.24 times that of the binding model.

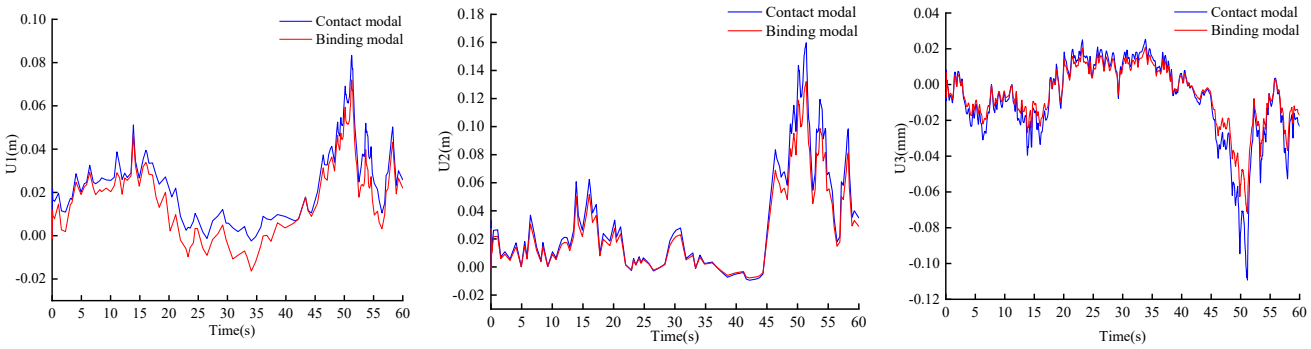

a) X-direction ***b) Y-direction*** ***c) Z-direction***

Fig. 7 – Displacement time history curves of film-tensioning line

The maximum displacement nodes on the film-tensioning line of both the contact and binding models are located in the shoulder region on the leeward side of the second film-tensioning line. As shown in the Fig. 7, the displacement at these peak nodes fluctuates with a similar variation trend observed for both models. The peak displacements for both the contact and binding models occur at 51.4 s.

At this time, the displacement components for the contact model are 83.3 mm in the x-direction, 159.8 mm in the y-direction, and 109.2 mm in the z-direction. For the binding model, the displacement components are 71.9 mm in the x-direction, 132.1 mm in the y-direction, and 72.1 mm in the z-direction. The maximum displacement components in the x, y, and z directions for the contact model are 1.16, 1.21, and 1.51 times those of the binding model, respectively.

CONCLUSIONS

This study developed dynamic equations of motion to analyze the wind-induced response of a flat-elliptical pipe greenhouse (FEPG) under fluctuating wind loads, using both contact and binding models. Key findings include:

(1) The contact model produces significantly higher peak stresses and displacements compared to the binding model, with the peak stress and displacement values in the contact model being up to 1.48 times and 2.93 times those in the binding model, respectively. These results underscore the importance of accounting for dynamic coupling effects between the film, frame, and film-tensioning lines.

(2) The inclusion of dynamic interactions under fluctuating wind loads is crucial for accurately predicting the structural response. The contact model, which incorporates these interactions, provides a more realistic representation of the greenhouse's behavior compared to the binding model, especially under extreme wind conditions.

(3) The results indicate that neglecting the dynamic coupling between structural components, particularly the film and film-tensioning lines, may lead to an underestimation of stress and displacement, potentially compromising the greenhouse's structural integrity.

Based on the findings, it is recommended that engineers adopt contact models for the design and analysis of greenhouses under fluctuating wind loads. This approach will more accurately predict the stresses and displacements, ensuring safer and more resilient structures, particularly in regions prone to extreme wind events. Based on the findings, it is recommended that engineers adopt contact models for the design and analysis of greenhouses under fluctuating wind loads. This approach will more accurately predict the stresses and displacements, ensuring safer and more resilient structures, particularly in regions prone to extreme wind events.

Future work should focus on: Comparative analysis of wind-induced responses under static and dynamic wind loads to assess the relative benefits of time-history analysis. Research on selecting and reinforcing materials based on dynamic responses observed in the contact model can further enhance the durability and safety of greenhouses. Conducting experiments to validate the simulation results and refine the dynamic models will help improve their predictive accuracy. By addressing these areas, the theoretical framework for FEPG wind response can be further refined, leading to more reliable and resilient greenhouse designs under fluctuating wind loads.

ACKNOWLEDGEMENTS

This study is supported by Natural Science Foundation of Heilongjiang Province of China (LH2019E072). All authors are grateful for this support.

REFERENCES

[1] Briassoulis D., Dougka G., Dimakogianni D., & Vayas I. (2016). Analysis of the collapse of a greenhouse with vaulted roof. *Biosystems Engineering*, Vol.151, pp. 495-509, England. DOI: https://doi.org/10.1016/j.biosystemseng.2016.10.018

[2] Davenport A.G. (1961). The spectrum of horizontal gustiness near the ground in high winds. *Quarterly Journal of the Royal Meteorological Society*, Vol. 87, No. 372, pp. 194-211, England. DOI: https://doi.org/10.1002/qj.49708737208

[3] Dougka G, Briassoulis D. (2020). Load carrying capacity of greenhouse covering films under wind action: Optimising the supporting systems of greenhouse films. *Biosystems Engineering,* Vol. 192, pp. 199-214, England. DOI:https://doi.org/10.1016/j.biosystemseng.2020.01.020

[4] Kim R.W., Lee I.B., Yeo U.H., & Lee S.Y. (2019). Evaluation of various national greenhouse design standards for wind loading. *Biosystems Engineering*, Vol. 188, pp. 136-154, England. DOI: https://doi.org/10.1016/j.biosystemseng.2019.10.004

[5] Kwon K.S., Kim D.W., Kim R.W., Ha T. & Lee I.B. (2016). Evaluation of wind pressure coefficients of single-span greenhouses built on reclaimed coastal land using a large-sized wind tunnel. *Biosystems Engineering*, Vol. 141, pp. 58-81, England. DOI: https://doi.org/10.1016/j.biosystemseng.2015.11.007

[6] Li X., Wang C., Jiang Y., Bai Y. (2022). Dynamic response analysis of a whole steel frame solar greenhouse under wind loads. *Scientific reports,* Vol. 12, pp. 1-12, England. DOI: https://doi.org/10.1038/s41598-022-09248-z

[7] MOHURD. (2012). *GB 50009-2012 Load code for the design of building structures.* (建筑结构荷载规范). Beijing, China: China Architecture & Building Press (in Chinese). DOI: https://www.mohurd.gov.cn/gongkai/fdzdgknr/tzgg/201207/20120723_210754.html.

[8] MOHURD. (2016). *GB/T 51183-2016 Code for the design load of horticultural greenhouse structures*. （农业温室结构荷载规范）. Beijing, China: China Planning Press (in Chinese) https://www.mohurd.gov.cn/gongkai/zhengce/zhengcefilelib/201702/20170214_230578.html.

[9] Ren J., Wang J., Guo S., Li X., Zheng K., & Zhao Z. (2019). Finite element analysis of the static properties and stability of a large-span plastic greenhouse. *Computers and Electronics in Agriculture,* Vol. 165, pp. 1-9, England. DOI: https://doi.org/10.1016/j.compag.2019.104957

[10] Reichrath S, Davies T W. (2002). Computational fluid dynamics simulations and validation of the pressure distribution on the roof of a commercial multi-span Venlo-type glasshouse. *Journal of Wind Engineering and Industrial Aerodynamics*, Vol. 90, pp: 139-149, England. DOI: https://doi.org/10.1016/S0167-6105(01)00184-2

[11] Richardson G. (1986). Wind loads on a full-scale film-plastic clad greenhouse: with and without Shelter from a wind break. *Journal of Wind Engineering and Industrial Aerodynamic*, Vol. 230, pp: 321-331, England. DOI: https://doi.org/10.1016/0167-6105(86)90052-8

[12] Ryu H.R., Choi M.K., Cho M.W., Yu I., Kim S. (2019). Damage index estimation by analysis of meteorological disasters on film plastic greenhouses. *International Journal of Agricultural and Biological Engineering*, Vol.12, pp: 58-63, China. DOI: 10.25165/j.ijabe.20191205.4493

[13] Wang C., Jiang Y., Wang T., Xu Z., Bai Y. (2022). Analysis of wind-induced responses of landing assembled Chinese solar greenhouses. *Biosystems Engineering*, Vol. 220, Issue 6, pp. 214-233, England. DOI: https://doi.org/10.1016/j.biosystemseng.2022.06.003

[14] Wang C., Xu Z., Jiang Y., Bai Y., & Wang T. (2023). Numerical analysis of static and dynamic characteristics of large-span pipe-framed plastic greenhouses. *Biosystems Engineering*, Vol. 232, No. 6, pp. 67-80, England. DOI: https://doi.org/10.1016/j.biosystemseng.2023.06.013

[15] Xie H., Wei C., Zheng X., Xu W. (2025). Stability analysis of flat-elliptical greenhouse skeleton considering initial geometrical imperfections. *INMATEH - Agricultural Engineering*, Vol. 76, No.2, pp. 369-379, Romania DOI: https://doi.org/10.35633/inmateh-76-31

[16] Wei C., Xie H., Zheng X., Xu W. (2025). Stress analysis of greenhouse film considering the contact between the film-tensioning strap, film, and frame. *INMATEH - Agricultural Engineering*, Vol. 77, No. 3, pp. 1200-1209, Romania. DOI: https://doi.org/10.35633/inmateh-77-97

[17] Wei C., Xie H., Zheng X., Xu W. (2025). Wind resistance performance analysis of a flat-elliptical pipe greenhouse frame. *INMATEH - Agricultural Engineering*, Vol. 77, No. 3, pp. 1249-1259, Romania. DOI: https://doi.org/10.35633/inmateh-77-101

[18] Wells D A., Hoxey R P. (1980). Measurements of wind loads on full-scale glasshouses. *Journal of Wind Engineering & Industrial Aerodynamics*, Vol. 1, pp: 139-167, England. DOI: https://doi.org/10.1016/0167-6105(80)90027-6

[19] Xie H., Wei C., Zheng X., Xu W. (2025). Stability analysis of flat-elliptical greenhouse skeleton considering initial geometrical imperfections. *INMATEH - Agricultural Engineering*, Vol. 76, No. 2, pp. 369-379, Romania. DOI: https://doi.org/10.35633/inmateh-76-31

[20] Xu Y., Li Y., Song H. (2023). Large-span M-shaped greenhouse with superior wind resistance and ventilation performances. *Journal of Wind Engineering and Industrial Aerodynamics*, Vol. 238, No. 105410, England. DOI: https://doi.org/10.1016/j.jweia.2023.105410